JASA ARTICLE

Solving time-independent inhomogeneous optoacoustic wave equation numerically with a modified Green's function approach

Ratan K. Saha[a)]
Department of Applied Sciences, Indian Institute of Information Technology Allahabad, Jhalwa, Allahabad 211015, India

ABSTRACT:
The purpose of the paper is twofold. First, a modified Green's function (MGF) approach is described for solving the time-independent inhomogeneous optoacoustic (OA) wave equation. The performance of this technique has been assessed with respect to the exact, traditional Born series and convergent Born series methods for an acoustically inhomogeneous spherical source. Second, we apply the same approach for calculating time domain signal from a blood vessel network consisting of an ensemble of acoustically homogeneous/inhomogeneous randomly positioned disks resembling cells. The predicted signals have been compared with those generated by the exact method and a freely available standard software. The OA spectra for a spherical source demonstrated excellent agreement with the exact results when sound-speed for the source was varied from −20% to 30% compared to that of the surrounding medium. The simulated OA signals also followed the same trend as that of the exclusively used software for the acoustically homogeneous blood vessel network. Future work will focus inclusion of a suitable phase factor within the MGF facilitating OA pulses building up at correct temporal locations for an acoustically inhomogeneous source.
 https://doi.org/10.1121/10.0005041

(Received 5 January 2021; revised 7 April 2021; accepted 6 May 2021; published online 8 June 2021)

[Editor: Bradley E. Treeby] Pages: 4039–4048

I. INTRODUCTION

The production of acoustic waves due to absorption of light is known as the optoacoustic/photoacoustic (OA/PA) effect. Essentially, short pulses of a laser beam irradiate a tissue. The tissue undergoes thermoelastic expansion, which results in emission of pressure waves. A biomedical imaging modality has been developed based on this phenomenon. It enjoys the advantages of optics and acoustics. Imaging of deep tissue regions with optical contrast at ultrasonic resolution is possible using this technique.[1–3] Currently, it operates in two modes—microscopy and tomography. On one hand, the OA microscopic technique focuses to image single cells, micro-vasculature, etc. On the other hand, the OA tomographic imaging attempts to form images of organs. Both the anatomical and functional information of the illuminated region can be gathered using these methods.

The generation and propagation of OA waves can be expressed using a time-dependent wave equation (under thermal and stress confinements). It can be easily converted into its time-independent form.[4] The time-independent OA wave equation is inherently an inhomogeneous Helmholtz equation. The right-hand side of this equation retains a term (i.e., the source term) and it is responsible for conversion of light energy into acoustic energy. The source term is nonzero inside the OA source, which may be acoustically homogeneous or inhomogeneous compared to the surrounding medium. An additional source term appears on the right-hand side in the wave equation for an inhomogeneous OA source accounting its mismatch in the sound-speed with respect to the ambient medium. The mismatch in sound-speed acts as a scattering potential. For example, sound-speed in red blood cells is approximately 10% higher than that of saline water and accordingly, scattering potential becomes nonvanishing.

The solutions to the time-independent inhomogeneous OA wave equation can be analytically obtained for objects with regular shapes (e.g., layer, infinite cylinder, sphere, etc.).[4] It is called the exact method. This procedure has been explored by us for computing OA signals from an ensemble of red blood cells approximated as spheres.[5] Two variants of the Born series method, referred to as the traditional Born series (TBS) and convergent Born series (CBS), have been applied to solve the same equation. Essentially, the OA field generated by an acoustically inhomogeneous disk was calculated using these techniques.[6,7] The Born series methods have been employed in optical scattering problems and also for seismic wavefield modelling in strongly scattering media.[8–11] The TBS procedure has been found to offer converging solutions when particle size and scattering potential are small. However, it cannot facilitate converging solutions if particle size and scattering potential are large. The CBS scheme provides converging solutions for arbitrarily large media.[8] The main advantage of these protocols is that OA fields can be computed for sources with irregular shapes. The major problem of these techniques is that they are computationally extensive and take a long time to numerically solve the wave equation (since they employ iterative approaches).

The Green's function (GF) method has been widely used by us to solve the OA wave equation for acoustically homogeneous sources mimicking biological targets.[12–15]

[a)]Electronic mail: ratank.saha@iiita.ac.in, ORCID: 0000-0001-7274-6707.

Various form factor models have been subsequently tested in order to extract the size and shape information of the source from the OA spectrum.[14] Mohajerani *et al.*, calculated the OA field produced by an extended illuminated region based on the GF approach and consequently, carried out image reconstruction. The modality is termed as the frequency domain OA tomography.[16,17] Baddour and Mandelis proposed a transfer function approach to solve inhomogeneous problems in OAs, and performed image reconstructions as well.[18,19] The time-dependent OA wave equation can also be solved numerically using the k-Wave toolbox which implements the pseudospectral method.[20] This toolbox has been extensively utilized in many studies.

Chu *et al.* used a modified GF (MGF) along with the Born approximation for solving the corresponding wave equation describing scattering process by a soft target in under water acoustics.[21] In this case, the acoustic property (i.e., sound-speed) of the OA source is incorporated within the GF while modeling the wave propagation inside the source. They revealed that it works well for predicting the scattered field generated by Zooplankton. This approach is referred to as the distorted wave Born approximation in the literature. We also implemented this approximation for investigating angular distributions of ultrasound scattering by soft targets resembling cells.[22]

The objective of the paper is to apply the MGF technique to solve the OA wave equation when sound-speed within a source (a spherical region) is different than that of the surrounding medium. Further, in this work, we consider the source term of the OA wave equation only (ignoring the term involving the scattering potential) and accordingly, compute the OA field using the MGF scheme and compare its performance with other methods. It is a very fast method and provides accurate estimation of the OA fields emitted by a spherical source with sound-speed contrast varying from −20% to 30%. The OA signal from an acoustically homogeneous/inhomogeneous solid disk has also been computed exploiting the MGF approach and thereafter the resultant signal from a blood vessel network in 2D (simulated by using a Monte Carlo algorithm by randomly placing solid disks imitating cells) has been calculated by linearly adding tiny signals from the individual disks. Such a simulated signal have been compared with those of exact and k-Wave methods.

The organization of the paper is as follows. Theoretical formulas are derived in Sec. II. The numerical methods for calculating the OA fields and time domain signals utilizing various frameworks and for different phantoms are presented in Sec. III. The simulation results are detailed elaborately in Sec. IV. Some important aspects of this study are highlighted in Sec. V. It also includes the conclusions of this study.

II. GOVERNING EQUATIONS

A. Exact analytical method

Consider a region that can absorb light and is embedded in an optically nonabsorbing fluid medium. The corresponding time-independent OA wave equation can be written as[4]

$$\nabla^2\psi(\mathbf{r}) + k_s^2\psi(\mathbf{r}) = \frac{i\mu\beta I_0\omega}{C_P} \text{ within the source,} \tag{1a}$$

$$\nabla^2\psi(\mathbf{r}) + k_f^2\psi(\mathbf{r}) = 0 \text{ in the surrounding medium,} \tag{1b}$$

where μ, β, and C_P denote the optical absorption coefficient, isobaric thermal expansion coefficient, and specific heat for the absorbing region, respectively; k_s and k_f indicate the wave numbers inside and outside the OA source, respectively. Here, ω and I_0 are the modulation frequency and the intensity of the incident light beam, respectively. A schematic diagram is shown in Fig. 1. The assumptions of thermal and stress confinements have been made while deriving Eq. (1). The OA source is acoustically inhomogeneous with respect to the surrounding medium (sound-speed is not the same), however, its physical properties do not vary spatially. Moreover, it is uniformly illuminated by the incident light beam.

The analytical solutions to Eq. (1) can be readily derived for regular objects (e.g., layer, infinite cylinder, sphere, etc.). Essentially, both equations are solved in an appropriate coordinate system and then the pressure and normal components of the particle velocity are matched at the boundary.[4] It works for any inhomogeneity of arbitrary strength (without size restriction). The OA field at a point $\mathbf{r}$ (outside the source) for a sphere of radius a becomes[4]

$$\psi_{ex}(\mathbf{r}) = \frac{i\mu\beta I_0\omega a^3}{C_P}\frac{e^{ik_f(r-a)}}{r} \times \left[\frac{[\sin(\hat{q}) - \hat{q}\cos(\hat{q})]}{\hat{q}^3[(1-\hat{\rho})\sin(\hat{q})/\hat{q} - \cos(\hat{q}) + i\hat{\rho}\hat{c}\sin(\hat{q})]}\right]. \tag{2}$$

Here, the dimensionless quantities are defined as $\hat{q} = k_s a$, $\hat{\rho} = \rho_s/\rho_f$, and $\hat{c} = c_s/c_f$. The density and sound-speed of the source region are indicated by ρ_s and c_s, respectively. The same quantities for the ambient medium are denoted by ρ_f and c_f, respectively. The subscript "ex" states the exact solution. In this work, Eq. (2) has been evaluated to compute the OA pressure produced by a spherical source.

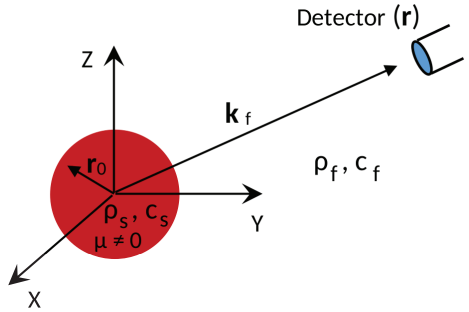

FIG. 1. (Color online) Demonstration of the OA set up.

https://doi.org/10.1121/10.0005041

B. Approximate methods

The OA wave equation as expressed in Eq. (1) after rearrangement of terms can be cast as[8]

$$\nabla^2\psi(\mathbf{r}) + (k_f^2 + i\epsilon)\psi(\mathbf{r}) = -S(\mathbf{r}) - V(\mathbf{r})\psi(\mathbf{r}), \tag{3}$$

where

$$S(\mathbf{r}) = \begin{cases} -\dfrac{i\mu\beta I_o\omega}{C_p} & \text{if } |\mathbf{r}| \le \text{a}, \\ 0 & \text{if } |\mathbf{r}| > \text{a} \end{cases} \tag{4}$$

and

$$V(\mathbf{r}) = \begin{cases} k_s^2 - k_f^2 - i\epsilon & \text{if } |\mathbf{r}| \le \text{a}, \\ -i\epsilon & \text{if } |\mathbf{r}| > \text{a}, \end{cases} \tag{5}$$

with $S(\mathbf{r})$ and $V(\mathbf{r})$ being the source term and the scattering potential, respectively. Similar equations can be found in acoustical, optical, and potential scattering problems.[23–25] The perturbation theory has been extensively used to solve these equations.[25] This method derives an approximate solution of a complex system in terms of a simple/known solution. It can give us sufficient insight regarding the dependence of the system on various parameters.

In this work, we use the GF method for solving Eq. (3). The numerical value of ϵ may be chosen as 0 or a small real number. These two cases are studied in detail in the following.

1. Case I ($\epsilon = 0$)

In this case, the solution to Eq. (3) becomes

$$\psi(\mathbf{r}) = \int_{V_{vol}} g_1(\mathbf{r}|\mathbf{r}_0)[S(\mathbf{r}_0) + V(\mathbf{r}_0)\psi(\mathbf{r}_0)]d^3\mathbf{r}_0, \tag{6}$$

where the integration is carried out over the volume of the source V_{vol} and $g_1(\mathbf{r}|\mathbf{r}_0)$ is the free space GF. The corresponding Helmholtz equation for $g_1(\mathbf{r}|\mathbf{r}_0)$ is[26]

$$\nabla^2 g_1(\mathbf{r}|\mathbf{r}_0) + k_f^2 g_1(\mathbf{r}|\mathbf{r}_0) = -\delta(\mathbf{r} - \mathbf{r}_0). \tag{7}$$

Here, δ is the Dirac delta function and $g_1(\mathbf{r}|\mathbf{r}_0)$ can be obtained as[26]

$$g_1(\mathbf{r}|\mathbf{r}_0) = \frac{e^{ik_f|\mathbf{r}-\mathbf{r}_0|}}{4\pi|\mathbf{r} - \mathbf{r}_0|}. \tag{8}$$

Equation (6) states that one needs to know the field inside the source in order to find out the same quantity outside the source. In reality, it is not known *a priory* posing a difficulty for performing the calculation. The standard approach is to start with an approximate field and expand Eq. (6) recursively to make accurate estimation of $\psi(\mathbf{r})$.

If the magnitude of the scattering potential is small, the contribution from the second term (i.e., the scattering potential) may be neglected and recursive expansion of Eq. (6) is not required. Further, the free space GF in three dimensions in the far field (i.e., $|\mathbf{r}| \gg |\mathbf{r}_0|$) becomes

$$g_1(\mathbf{r}|\mathbf{r}_0) \approx \frac{e^{ik_f r}}{4\pi r} e^{-i\mathbf{k}_f\cdot\mathbf{r}_0}, \tag{9}$$

where $\mathbf{k}_f$ defines the direction of measurement (see Fig. 1) and hence the solution becomes

$$\begin{aligned}\psi_{gf}(\mathbf{r}) &\approx -\int_{V_{vol}} \frac{i\mu\beta I_o\omega}{C_p}\frac{e^{ik_f r}}{4\pi r} e^{-i\mathbf{k}_f\cdot\mathbf{r}_0} d^3\mathbf{r}_0 \\ &= -\frac{i\mu\beta I_o\omega a^3}{C_p}\frac{[\sin(k_f a) - k_f a\cos(k_f a)]}{k_f^3 a^3}\frac{e^{ik_f r}}{r},\end{aligned} \tag{10}$$

where the subscript gf represents the GF. Note that this approach treats the source region as acoustically homogeneous compared to the surrounding medium (i.e., sound-speed contrast is equal to zero).

Chu *et al.*, in the context of acoustic scattering by Zooplankton, approximated the GF in the following manner:[21]

$$g_1(\mathbf{r}|\mathbf{r}_0) \approx \frac{e^{ik_f r}}{4\pi r} e^{-i\mathbf{k}_s\cdot\mathbf{r}_0}. \tag{11}$$

This approach included the acoustical property of the inhomogeneity efficiently compensating the phase mismatch arising due to sound-speed contrast and provided accurate prediction of frequency dependent backscatter amplitude.[21,22] This is referred to as the MGF in the text. For such a GF, one calculates

$$\begin{aligned}\psi_{mgf}(\mathbf{r}) &\approx -\int_{V_{vol}} \frac{i\mu\beta I_o\omega}{C_p}\frac{e^{ik_f r}}{4\pi r} e^{-i\mathbf{k}_s\cdot\mathbf{r}_0} d^3\mathbf{r}_0 \\ &= -\frac{i\mu\beta I_o\omega a^3}{C_p}\frac{[\sin(k_s a) - k_s a\cos(k_s a)]}{k_s^3 a^3}\frac{e^{ik_f r}}{r}.\end{aligned} \tag{12}$$

It is interesting to note that this approach reproduces approximately the same solution as that of the exact method [compare Eqs. (2) and (12)]. In this work, Eqs. (10) and (12) have been computed to estimate the OA pressure generated by a spherical source.

2. Case II ($\epsilon \neq 0$)

The solutions given in Eqs. (10) and (12) are far field solutions. Therefore, in general, they may not be suitable if measurement is carried out close to the source. Furthermore, the contribution of the scattering potential arising from the sound-speed mismatch has been ignored. In order to address these issues, we chose $\epsilon \neq 0$ and proceed in the following manner.

In this case, the solution to Eq. (3) becomes

$$\psi(\mathbf{r}) = \int_{V_{vol}} g_2(\mathbf{r}|\mathbf{r}_0)[S(\mathbf{r}_0) + V(\mathbf{r}_0)\psi(\mathbf{r}_0)]d^3\mathbf{r}_0, \tag{13}$$

where $g_2(\mathbf{r}|\mathbf{r}_0)$ obeys

$$\nabla^2 g_2(\mathbf{r}|\mathbf{r}_0) + (k_f^2 + i\epsilon) g_2(\mathbf{r}|\mathbf{r}_0) = -\delta(\mathbf{r} - \mathbf{r}_0), \tag{14}$$

obtaining

$$g_2(\mathbf{r}|\mathbf{r}_0) = \frac{e^{i\sqrt{k_f^2 + i\epsilon}|\mathbf{r}-\mathbf{r}_0|}}{4\pi|\mathbf{r} - \mathbf{r}_0|}. \tag{15}$$

Note that $g_2(\mathbf{r}|\mathbf{r}_0)$ decays exponentially with distance for finite ϵ and thus represents the GF for lossy unbounded medium. The corresponding expression in the Fourier domain in terms of Fourier transformed coordinates ($\mathbf{p}$) becomes

$$\tilde{g}_2(\mathbf{p}) = \frac{1}{(|\mathbf{p}|^2 - k_f^2 - i\epsilon)}. \tag{16}$$

The convolution sum presented in Eq. (13) can be cast in the matrix form yielding

$$\psi = GS + GV\psi, \tag{17}$$

where $G = \mathcal{F}^{-1}\tilde{g}_2(\mathbf{p})\mathcal{F}$, with $\mathcal{F}$ and $\mathcal{F}^{-1}$ as the forward and inverse Fourier transform operators, respectively. Equation (17) can be recursively expanded providing

$$\psi_{TBS} = [1 + GV + GVGV + \cdots]GS. \tag{18}$$

This is the well-known TBS. The infinite series converges if GV is less than unity.[8] The TBS method is capable of providing reliable solutions to the inhomogeneous Helmholtz equation for small objects having weak scattering potential. Equation (18) has been calculated herein numerically to estimate the OA pressure produced by a light absorbing sphere.

Let us consider that both sides of Eq. (17) are multiplied by a preconditioner γ and thus one attains[8]

$$\gamma\psi = \gamma GV\psi + \gamma GS. \tag{19}$$

Equation (19) after rearrangement of terms can be written as

$$\psi_{CBS} = M\psi_{CBS} + \gamma GS, \tag{20}$$

where $M = \gamma GV - \gamma + 1$. Similar to Eq. (18), an infinite series can also be derived through recursive expansion of Eq. (20) as

$$\psi_{CBS} = [1 + M + M^2 + \cdots]\gamma GS. \tag{21}$$

The above series converges if $M < 1$. It has been shown that this infinite series converges for all structures when $\gamma = (i/\epsilon)V(\mathbf{r})$ and $\epsilon \geq \max|k_s^2 - k_f^2|$.[8] The CBS technique essentially extends the validity domain of the TBS method facilitating converging results for large structures as well.[8] Equation (21) has been applied herein to compute the OA field generated by an acoustically homogeneous/inhomogeneous source.

III. NUMERICAL IMPLEMENTATION

A. Computation of OA pressure for a spherical source

1. Physical properties of the source

The OA field was computed for a homogeneous sphere of radius $a = 5\,\mu$m and at a distance $r = 15.5\,\mu$m from the center of the source. This OA source essentially mimicked a cell. Note that studies on OA emission from single cells may play a vital role to develop an OA technology for cell characterization.[14] The density for the source and the surrounding medium was fixed at $\rho_s = \rho_f = 1000\,\text{kg/m}^3$. The sound-speed of the ambient medium was chosen as $c_f = 1500\,$m/s. These numerical values are similar to those of tissue media.[6,7] The sound-speed for the source region was gradually decreased from $c_s = 1950$ to 1200 m/s with a decrement of 150 m/s. Therefore, sound-speed of the source region was varied from 30% to −20% compared to the surrounding medium. This range was arbitrarily fixed. The thermo-opto-mechanical parameters were taken as constants such as $I_0 = 1$, $\mu = 1$, $\beta = 1$, $C_P = 1$. The magnitudes of these parameters do not change the features of the OA spectrum rather control its amplitude.

2. Contribution from the source term only

The OA pressure was calculated over a large frequency band from $f = 29.3$ to 1552.7 MHz with a step size of 29.3 MHz. The lower limit of the frequency band was determined from the size of the computational domain. Many OA experiments in the single cell level were carried out in the GHz range and based on this, the upper limit was fixed.[27] Equations (2), (10), and (12) were computed to obtain the OA pressure for the exact GF and MGF methods, respectively, for a spherical source.

3. Implementation of the Born series methods

The details an implementation of the Born series methods (for 2D) can be found in the literature.[6,7] However, for the sake of completeness the same has been briefly described here (for 3D). The three-dimensional computational domain was discretized into $512 \times 512 \times 512$ voxels with grid size $dx = dy = dz = 100$ nm. The numerical value for ϵ was considered as $\epsilon = 0.6k_f^2$.[7] Note that this choice satisfied $\epsilon \geq \max|k_s^2 - k_f^2|$ for all cases (i.e., when sound-speed varied from $c_s = 1950$ to 1200 m/s). The spatial distributions of the source and the scattering regions were initialized as per Eqs. (4) and (5), respectively. The source was placed at the central region of the computational domain (see Fig. 2). The GF (in the frequency domain) was evaluated at each grid point as per Eq. (16) and was stored in a 3D matrix. The initial pressure values in the two methods were taken as

$$\psi_{TBS_0}(\mathbf{r}) = \text{ifft}_3\left[\tilde{g}_2(\mathbf{p})\text{fft}_3 S(\mathbf{r})\right] \tag{22}$$

and

$$\psi_{CBS_0}(\mathbf{r}) = \gamma(\text{ifft}_3\left[\tilde{g}_2(\mathbf{p})\text{fft}_3 S(\mathbf{r})\right]), \tag{23}$$

https://doi.org/10.1121/10.0005041

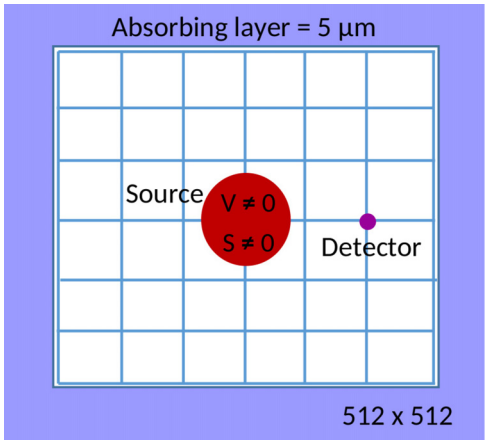

FIG. 2. (Color online) Schematic of the computational domain in 2D.

respectively. Here, fft_3 and ifft_3 represent forward and inverse fast Fourier transforms in 3D. All the multiplications were performed element wise.

The iterative computation was started after that. For example, the pressure values at the grid points at the $(n+1)$th step were calculated using those values of the nth step in the following manner:

$$\psi_{TBS_{n+1}}(\mathbf{r}) = \text{ifft}_3\left[\tilde{g}_2(\mathbf{p})\text{fft}_3\left[S(\mathbf{r}) + V(\mathbf{r})\psi_{TBS_n}(\mathbf{r})\right]\right], \tag{24}$$

in the case of the TBS algorithm. The same procedure was also adapted for the CBS algorithm as given below:

$$\psi_{CBS_{n+1}}(\mathbf{r}) = \psi_{CBS_n}(\mathbf{r}) - (i/\epsilon)V(\mathbf{r})\Big(\psi_{CBS_n}(\mathbf{r}) - \text{ifft}_3\left[\tilde{g}_2(\mathbf{p})\text{fft}_3\left[S(\mathbf{r}) + V(\mathbf{r})\psi_{CBS_n}(\mathbf{r})\right]\right]\Big). \tag{25}$$

It might be mentioned here that after each step the pressure values were multiplied by an attenuation mask defined as

$$AtnMsk(\mathbf{r}) = \begin{cases} e^{-\sqrt{\epsilon}|\mathbf{r}|} & \text{if } |\mathbf{r}| \text{ lies within the ABL,} \\ 1 & \text{otherwise.} \end{cases} \tag{26}$$

Here, ABL means the absorbing layer (see Fig. 2). Therefore, ψ_{n+1} was multiplied by $AtnMsk(\mathbf{r})$ and the product was considered as the input for Eq. (24) or for Eq. (25). In other words, ψ_n was updated as, $\psi_n = AtnMsk\psi_{n+1}$. The pressure waves were absorbed within the absorbing layer and thus reflection of the waves could not occur from the boundaries. Moreover, it greatly suppressed the effect of periodic boundary conditions inherently embedded in the implementation of the fast Fourier transform algorithm. After each iteration total error was determined,

$$\text{Total error} = \sum_{m=1}^{512} \frac{|\psi_{n+1}(256,m,256) - \psi_n(256,m,256)|}{|\psi_n(256,m,256)|}. \tag{27}$$

The iterative procedure was stopped when the total error became $\leq 10^{-4}$. It was also stopped if this condition was not met even after 1500 steps. The numerical codes implementing the TBS and CBS algorithms were written in MATLAB. The codes were executed in a virtual machine [CentOS, Intel Core Processor (Broadwell, IBRS)] working at 2.19 GHz, with 256 GB RAM and 80 cores. Sample codes (for 2D) can be found elsewhere.[28]

B. Computation of OA signal for a blood vessel network

The next step was to calculate the OA signal generated by a blood vessel network in the framework of the MGF. The blood vessel network was assumed to be filled with solid disks (mimicking erythrocytes). The OA signals from individual disks were simulated and summed up to obtain the resultant signal. The procedure is detailed below.

1. Construction of a blood vessel network

At first a binary image of a blood vessel network was scanned at 600 dots per inch. The scanned area was $20 \times 20\,\text{mm}^2$ and the matrix size was 473×473 with pixel size $dx = dy = 42.33\,\mu\text{m}$. A numerical value of 1 was assigned to the grid points inside the blood vessel and 0 was tagged otherwise. The number of grid points inside the blood vessel was found to be 19 215 out of 223 729 points. Therefore, the area covered by the blood vessel was about $34.4\,\text{mm}^2$. This area was populated with solid disks with radius $\alpha = 2.75\,\mu\text{m}$. The number of disks was $N = 579\,762$ so that the hematocrit level became about 0.4. These disks were placed within the blood vessel randomly using a Monte Carlo technique known as the random sequential adsorption technique.[29–31] Essentially, the entire image was divided into 473 rectangular strips with area $20\,000 \times 42.33\,\mu\text{m}^2$. The pixels belonging to the blood vessel within each strip were filled up with the disks. The disks were placed in such a way that they did not overlap. The disks situated at a boundary of a strip also maintained the nonoverlapping condition with those of the adjacent strip. In this way, the coordinates of the disks were generated and utilized while computing the OA signal. A MATLAB code was written for this purpose. The execution time was about 80 s in the same virtual machine.

Figure 3 displays the constructed blood vessel which mimics well the actual structure. The figure in inset exhibits spatial organization of some particles situated within the blue box. It essentially demonstrates the discrete particle nature of the vessel. This approach retains the structural details of the blood vessel network in the cellular level.

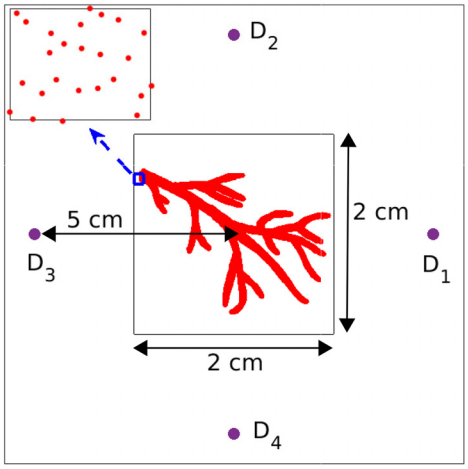

FIG. 3. (Color online) Construction of the blood vessel network phantom using the Monte Carlo method. The inset exhibits spatial distribution of a small number of particles located inside the blue box. The solid dots represent point detectors positioned at D_1, D_2, D_3, and D_4 locations.

2. OA signal calculation

The MGF in 2D far away from the source point is given by

$$g_1(\mathbf{r}|\mathbf{r}_0) \approx \frac{i}{4}\sqrt{\frac{2}{\pi k_f r}}e^{i(k_f r-\pi/4)}e^{-i\mathbf{k}_s\cdot\mathbf{r}_0}. \tag{28}$$

Accordingly, the OA field generated by a solid disk can be calculated as

$$\begin{aligned}\psi_{mgf}^{disk}(\mathbf{r}) &\approx -\int_{A_{area}}\frac{i\mu\beta I_o\omega}{C_p}\frac{i}{4}\sqrt{\frac{2}{\pi k_f r}}e^{i(k_f r-\pi/4)}e^{-i\mathbf{k}_s\cdot\mathbf{r}_0}d^2\mathbf{r}_0\\ &= \frac{\mu\beta I_o\omega}{4C_p}\sqrt{\frac{2}{\pi k_f}}\frac{2\pi\alpha J_1(k_s\alpha)}{k_s}\frac{e^{i(k_f r-\pi/4)}}{\sqrt{r}},\end{aligned} \tag{29}$$

where J_1 is the Bessel function of the first kind of order unity; α is the radius of the disk and the integration is carried out over the area of the source (A_{area}). Consider that there are L number of disks within the region of interest and all of them are uniformly illuminated by the incident laser beam. The corresponding OA signal for a delta function heating pulse can be computed as

$$\begin{aligned}\psi_{mgf}^{many-disks}(\mathbf{r},t) \approx \frac{\mu\beta F}{4C_p}\int_{-\infty}^{\infty}\sum_{l=1}^{L}\Bigg[\sqrt{\frac{2}{\pi k_f}}\frac{\alpha J_1(k_s\alpha)}{k_s}\\ \times\omega e^{-i\mathbf{k}_f\cdot\mathbf{r}_l}\frac{e^{i(k_f r-\omega t-\pi/4)}}{\sqrt{|\mathbf{r}-\mathbf{r}_l|}}\Bigg]d\omega,\end{aligned} \tag{30}$$

where F is the fluence of the incident light beam. The acoustic inhomogeneity of each source is taken into consideration in this approach. Equation (30) provides the theoretical framework for calculating the OA signal for a collection of disks randomly positioned in a blood vessel network.

The OA signals for such an extended source were computed at four detector locations (i.e., at D_1, D_2, D_3, and D_4) for $r = 50$ mm. At first the OA signal was calculated for a source particle and stored as a reference signal. The frequencies contributed to the signal were taken as 1 kHz to 1000 MHz with a step of 10 kHz. The sampling frequency was chosen as 2000 MHz providing the sampling interval as $dt = 0.5$ ns. The signals for all other particles were computed by using proper scaling and shifting of the reference OA signal. All such signals were linearly added to obtain the resultant signal. The resultant signal was filtered using a cosine Gabor filter which mimicked the frequency response of a transducer with centre frequency of 5 MHz and 70% as the −6 dB bandwidth and then decimated 40 times. Final sampling interval became $dt = 20$ ns. The OA signals were calculated and stored for two cases, $c_s = 1500$ and 1800 m/s, respectively. The OA signal was stored from t = 0 to 60 μs. Similar signals were also generated using the exact method for comparison.[29]

3. OA signal computation with the k-Wave toolbox

The binary image of the same blood vessel network was loaded in the k-Wave simulation toolbox. The computational domain was taken as 1101×1101 pixels with $dx = dy = 100\,\mu$m. The perfectly matched layer was 2 mm thick. The center frequency and −6 dB bandwidth of the sensors were fixed at 5 MHz and 70%, respectively. The effective sound-speed for the source region was assigned to be $c_{eff} = 1500$ and 1600 m/s for the first and second cases, respectively. It could be defined in terms of density (ρ_{eff}) and compressibility (κ_{eff}) as $c_{eff} = 1/\sqrt{\rho_{eff}\kappa_{eff}}$. For the second case, the density and compressibility were taken as $\rho_{eff} = 1000\,\text{kg/m}^3$ and $\kappa_{eff} = 0.4\kappa_{disk} + 0.6\kappa_{medium} = 3.90 \times 10^{-10}\,\text{m}^2/\text{N}$, where $\kappa_{disk} = 3.09 \times 10^{-10}\,\text{m}^2/\text{N}$ and $\kappa_{medium} = 4.44 \times 10^{-10}\,\text{m}^2/\text{N}$. The OA signals for these two settings were computed and compared with those of the previous approaches. The sampling interval was found to be $dt = 20$ and 18.75 ns in these two cases, respectively, so that the Courant-Friedrichs-Lewy number became fixed at 0.3. It can be mentioned here that k-Wave results are not dependent on the choice of numerical parameters (e.g., dx and dt).

IV. NUMERICAL RESULTS

Figure 4 displays how the OA pressure amplitude generated by a spherical source (radius, $a = 5.0\,\mu$m) varies with frequency over a bandwidth ≈ 29 to 1550 MHz. The sound-speed of the source region was gradually changed from $c_s = 1950$ to 1200 m/s in (a) to (f), respectively, with a decrement of 150 m/s. However, the same quantity for the ambient medium was fixed at $c_f = 1500$ m/s. The OA spectra provided by the exact, TBS, CBS, GF, and MGF methods are drawn in each figure. Further, each figure is split into two panels to improve the clarity of each image. It can be seen from Figs. 4(b1)–4(e1) [i.e., the upper panel in each figure] that the TBS and CBS methods provide accurate estimates of the OA pressure over the entire frequency range.

https://doi.org/10.1121/10.0005041

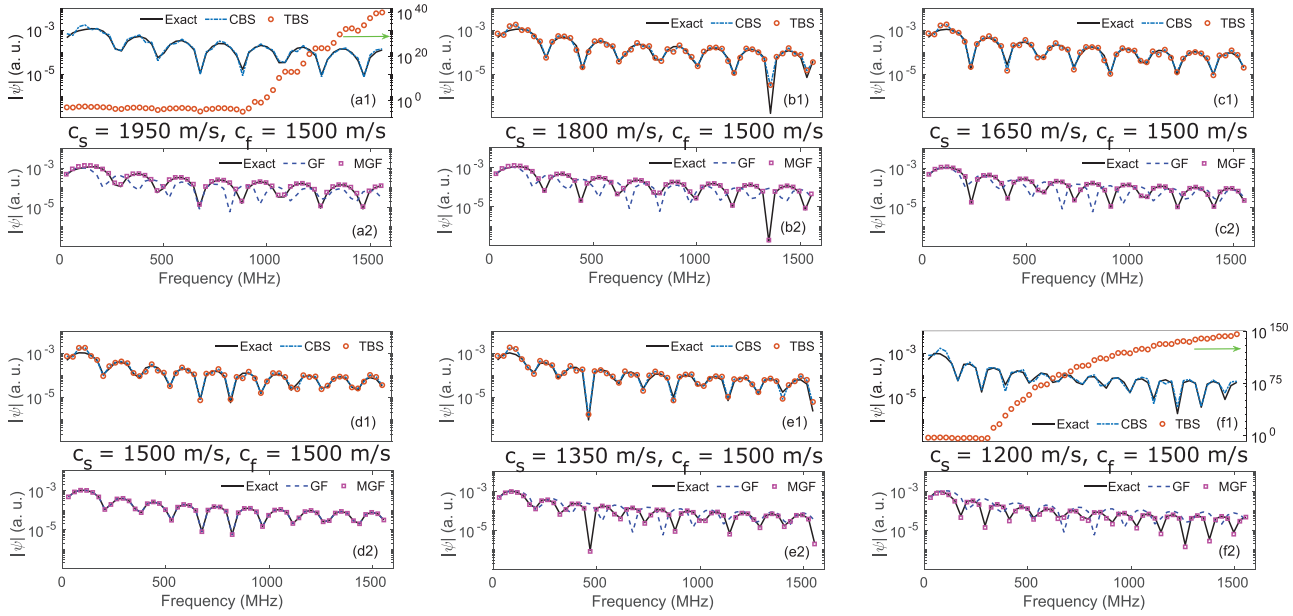

FIG. 4. (Color online) Plots of the OA spectra computed for a spherical source (with radius, $a = 5.0\,\mu$m) under different sound-speed contrast conditions. (a)–(f) Sound-speed for the source region was decreased from $c_s = 1950$ to 1200 m/s, respectively, but c_f was fixed at $c_f = 1500$ m/s. The graphs for the exact, TBS, and CBS methods are presented in the upper panel in each figure [(a1)–(f1)]; the same for the GF and MGF techniques along with the exact method are drawn in the lower panel in each figure [(a2)–(f2)]. The scale for the TBS algorithm is along the right y axis in (a1) and (f1).

The TBS technique cannot produce converging results when $c_s = 1950$ m/s and $f \geq 908$ MHz as shown in Fig. 4(a1). Similar observation can also be made when $c_s = 1200$ m/s and $f \geq 352$ MHz [see Fig. 4(f1)]. In other words, the TBS algorithm remains valid when the size parameter remains $k_f a < 19$ and 7, respectively. The CBS protocol still stands valid and thus extends the validity of the Born series method. It may also be mentioned here that the number of oscillations increases as the sound-speed of the source region is decreased [compare Figs. 4(a1) and 4(f1)].

Figures 4(a2)–4(f2) [i.e., the lower panel in each figure] confirm that magnitudes and locations of peaks and dips of the OA lines provided by the MGF scheme demonstrate perfect match with those of the exact technique. This is true for all sound-speed mismatch conditions. The minima positions in case of the GF method appear slightly earlier if $c_s > c_f$ and little later if $c_s < c_f$ than those of the exact procedure. For example, the first peak occurs at 88 MHz earlier and 30 MHz later than those of the exact curve in Figs. 4(a2) and 4(f2), respectively.

The OA signals generated by the blood vessel network and captured at two detector locations (D_3 and D_4, see Fig. 3) are shown in Fig. 5. Figures 5(a1) and 5(a2) present the OA signals computed using the exact and MGF methods, respectively. Both the signals (from acoustically inhomogeneous and homogeneous blood vessels) are shown in each figure. The signals are not visually distinguishable and the one is lying on the other. However, the signals provided by the k-Wave technique are not overlapping (marked by the black arrows) at all time points as shown in Fig. 5(a3). This is expected because sound-speeds inside the source in these cases are not the same. The OA signals recorded at the D_4 location are shown in Figs. 5(b1), 5(b2), and 5(b3) and similar observations can be made. Overall agreement between the exact and MGF results validates the later method.

It is clear from the above that the OA spectra and signals for the exact and MGF methods agree well. However, the OA signals (for these techniques) differ with respect to those of the k-Wave method (see Fig. 5). We have studied this aspect in details and the results are shown in Fig. 6. Essentially, the OA signal measured at a distance 5 cm from the center of an inhomogeneous source (a disk with radius, $\alpha = 5$ mm) has been compared with that of a homogeneous disk in each method. Figure 6(a) shows that the OA signals from the front surface for these sources occur at the same location but the second pulse for the inhomogeneous disk leads a bit than that of the homogeneous disk. This is expected because sound-speed inside the source region is higher than that of the extra cellular matrix for the inhomogeneous source. The pulses (for the inhomogeneous disk) computed by the MGF method appear little later/earlier for the front/back surface in comparison to that of the homogeneous disk as shown in Fig. 6(b). The k-Wave signals manifest better match with the exact signals [compare Figs. 6(a) and 6(c)] in comparison to the MGF scheme.

V. DISCUSSION AND CONCLUSIONS

In this work, an MGF approach has been deployed to solve the time-independent inhomogeneous OA wave equation. This equation arises in practice if the sound-speed of the source region differs from those of the ambient medium. The MGF retains a term which includes the acoustic property (i.e., sound-speed) of the source so that wave propagation inside the inhomogeneity becomes medium dependent.

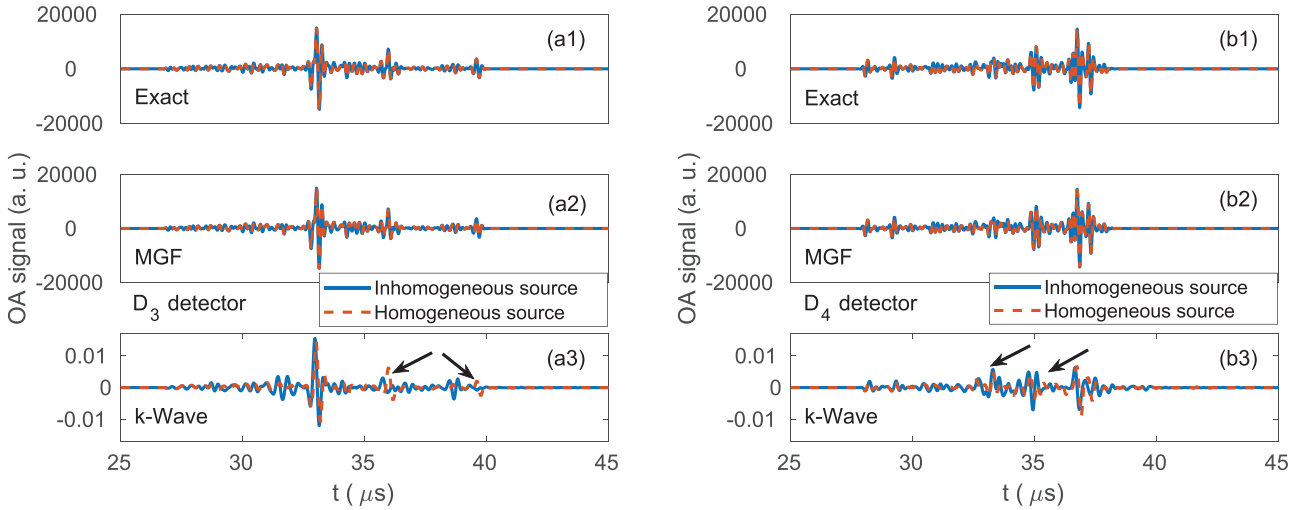

FIG. 5. (Color online) Comparison of the OA signals collected from the blood vessel network phantom. (a1)–(a2) Plots of the OA signal generated by the exact and MGF methods, respectively and detected at the D_3 location (for the inhomogeneous source—$c_s = 1800$ m/s and $c_f = 1500$ m/s; for the homogeneous source—$c_s = c_f = 1500$ m/s). (a3) Same as (a1) but for the k-Wave technique, respectively (for the inhomogeneous source—$c_{eff} = 1600$ m/s and $c_f = 1500$ m/s; for the homogeneous source—$c_{eff} = c_f = 1500$ m/s). (b1)–(b3) Same as (a1)–(a3), respectively, but the signals are recorded by the detector placed at D_4. Two black arrows in (a3) and (b3) represent the approximate locations where the signals from the inhomogeneous source precedes than that of the homogeneous source.

The OA spectra provided by the MGF and exact techniques exhibit excellent match for a spherical source (see Fig. 4). It has been observed that the TBS method can facilitate a converging result up to $k_f a = 32$ if mismatch in sound-speed is $> -11\%$ and $<21\%$. The CBS scheme works faithfully even beyond these limits.

The exact GF and MGF methods took less than 10 ms to compute an OA spectrum for a spherical source. The execution time for the TBS algorithm (for $512 \times 512 \times 512$ as the size of the computational domain) was about 31 h, 7 h, 4 h 50 min, 4 h 40 min, 5 h 20 min, and 54 h for $c_s = 1950$, 1800, 1650, 1500, 1350, and 1200 m/s, respectively. The same quantity for the CBS scheme was approximately 6 h 18 min, 5 h 30 min, 5 h 45 min, 6 h, 5 h, and 7 h 25 min, respectively. The average time for each k-Wave simulation was nearly 12 h 30 min (nearly 11 h 30 min, 14 h 30 min, 12 h 20 min, 11 h 30 min, 11 h 54 min, and 13 h 55 min, respectively). We executed the k-Wave simulations for the same computational domain to compare calculation efficiency of different methods, but the corresponding OA spectra have not been shown in this work. The frequency content of OA signals provided by the k-Wave method was much greater than the Born series algorithms. The MGF approach is undoubtedly preferable for rapid computation of the OA field.

A limitation of the MGF method is that the pulses (corresponding to the boundaries of the source) do not appear at the same locations as those of the exact method. It occurs because of an inherent deficiency of this approach.[21] It fails to predict the imaginary part of the OA spectrum. The volume integration in Eq. (12) provides a real quantity and thus does not contain any phase part which results in small shifting of the pressure pulses in the time domain [compare Figs. 6(a) and 6(b)]. However, the k-Wave software regenerates the exact result in a better manner [compare Figs. 6(a) and 6(c)]. Chu *et al.* designed a phase compensated distorted wave Born approximation method so that phase part could be restored well.[21] A similar approach may be adapted in OAs too in future facilitating accurate estimation of the time domain signal.

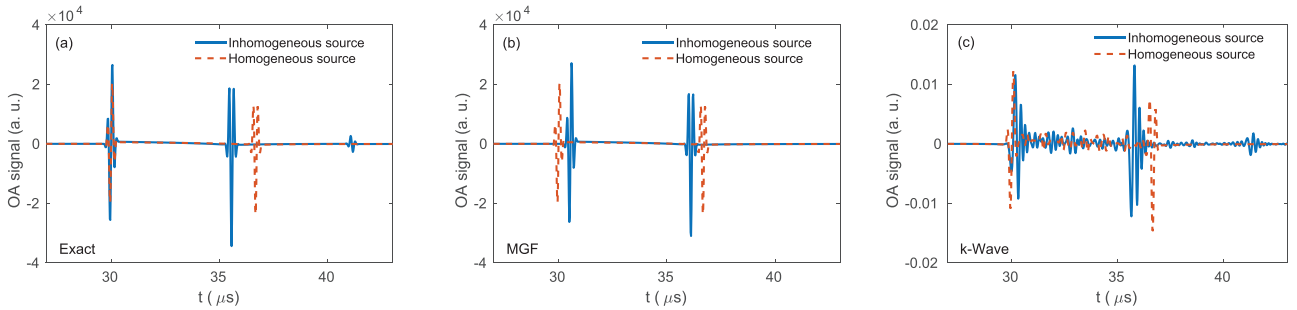

FIG. 6. (Color online) (a) Simulated OA signals using the exact method for a source (disk) with $a = 5$ mm and computed at a distance 5 cm from the center of the source. For the inhomogeneous source, $c_s = 1800$ m/s and for the homogeneous source, $c_s = 1500$ m/s. In both cases, the source is surrounded by a medium with $c_f = 1500$ m/s. (b)–(c) Same as (a) but generated by the MGF approach and the k-Wave toolbox, respectively.

https://doi.org/10.1121/10.0005041

The amount of shift of the OA pulse from the distal surface of the source (from the detector) is distinguishably visible in Fig. 6 because we considered sufficiently large object with 20% sound-speed contrast compared to the surrounding medium. Analogous change may not be visible for a small object (e.g., disk mimicking an erythrocyte) for which pulses from the boundaries would be overlapping. It may be speculated that because of this reason no deviation in the resultant OA signal is observed for the inhomogeneous source compared to that of the homogeneous source [see Figs. 5(a1), 5(a2), 5(b1), and 5(b2)]. However, the OA signal computed by the k-Wave method for the inhomogeneous source exhibits a small deviation compared to that of homogeneous source [see Figs. 5(a3) and 5(b3), marked by the black arrows]. This is expected because the k-Wave toolbox splits the source region into pixels which are extended objects compared to a disk resembling an erythrocyte.

The Monte Carlo method known as the random sequential adsorption technique was implemented herein to create a blood vessel network phantom. In this scheme, each erythrocyte was modeled as a solid disk and was placed randomly within the blood vessel. Once a disk was positioned inside the vessel, via a valid throw, the coordinates of the disk became fixed and fine tuning of its location was not possible. Tissue simulation using this approach works well for sparse medium, however, may become difficult for a dense medium (e.g., at 50% hematocrit). The Metropolis algorithm can also be used to construct a tissue realization.[32] In this algorithm, the position coordinates of the disks are continuously updated in order to achieve minimum energy state and thus provides an efficient way for tissue simulation. In general, OA signal simulation by exploiting the discrete particle approach (i.e., linearly superimposing the tiny signals from the individual disks) in conjunction with tissue simulation exploring the Monte Carlo technique offers an alternative and faster way with respect to the extensively used k-Wave toolbox method.

As mentioned earlier, many groups are trying to develop an imaging modality referred to as the frequency domain OA tomography. It has several advantages over the conventional time domain OA tomography.[16,17] So far theoretical/numerical studies related to frequency domain OA tomography have considered acoustically homogeneous region of interest only and therefore, the simple GF approach has been good enough for evaluating the OA field around the imaging region. We anticipate that the MGF method can be deployed for dealing imaging regions with heterogeneous sound-speed distribution and computing accurate OA fields. Furthermore, in this work, we simulated the OA spectra of a spherical source under various sound-speed contrast conditions (see Fig. 4). However, we neglected scattering of the incident light beam while calculating the OA fields for such micron-sized objects. It would be interesting in future to study the impact of light scattering on OA emission by such a source.

In conclusion, in this work, we apply an MGF approach to solve the inhomogeneous OA wave equation (i.e., sound-speed of the source region differs from that of the ambient medium). This approach incorporates acoustic property of the source region while modeling the wave propagation inside the source. It considers the contribution of the source term only (ignoring the contribution from the scattering potential) when calculating the pressure field generated by an OA source. The computed OA spectra for a spherical source have been compared with the corresponding results provided by the exact, Born series, and GF methods. The simulated OA spectra for the MGF protocol exhibit perfect match with those of the exact method when sound-speed contrast of the source medium is varied from −20% to 30% with respect to the surrounding medium. Therefore, accurate and rapid estimation of the OA pressure field is possible using this approach for an acoustically inhomogeneous source. Further investigation is required to introduce additional phase factor within the MGF so that time domain OA signal features can be produced at appropriate temporal locations.

ACKNOWLEDGMENT

The computational results reported in this work were performed on the Central Computing Facility of IIITA, Allahabad. R.K.S. would like to thank Dr. Phaneendra K Yalavarthy of MIG, IISc for his hospitality in summer 2017 when initial work on the Born series methods was carried out. The author declares no conflicts of interest.

[1]L. V. Wang, *Photoacoustic Imaging and Spectroscopy* (CRC Press, Boca Raton, 2017).
[2]L. V. Wang and J. Yao, "A practical guide to photoacoustic tomography in the life sciences," Nat. Methods **13**(8), 627–638 (2016).
[3]P. K. Upputuri and M. Pramanik, "Recent advances toward preclinical and clinical translation of photoacoustic tomography: A review," J. Biomed. Opt. **22**(4), 041006 (2016).
[4]G. Diebold, T. Sun, and M. Khan, "Photoacoustic monopole radiation in one, two, and three dimensions," Phys. Rev. Lett. **67**(24), 3384–3387 (1991).
[5]R. K. Saha and M. C. Kolios, "A simulation study on photoacoustic signals from red blood cells," J. Acoust. Soc. Am. **129**(5), 2935–2943 (2011).
[6]A. Kaushik, P. K. Yalavarthy, and R. K. Saha, "Convergent born series improves the accuracy of numerical solution of time-independent photoacoustic wave equation," J. Mod. Opt. **67**(9), 849–855 (2020).
[7]R. K. Saha, "Numerical solution to the time-independent inhomogeneous photoacoustic wave equation using the born series methods," J. Opt. Soc. Am. A **37**(12), 1907–1915 (2020).
[8]G. Osnabrugge, S. Leedumrongwatthanakun, and I. M. Vellekoop, "A convergent born series for solving the inhomogeneous Helmholtz equation in arbitrarily large media," J. Comput. Phys. **322**, 113–124 (2016).
[9]B. Krüger, T. Brenner, and A. Kienle, "Solution of the inhomogeneous Maxwell's equations using a born series," Opt. Express **25**(21), 25165–25182 (2017).
[10]X. Huang, M. Jakobsen, and R.-S. Wu, "On the applicability of a renormalized born series for seismic wavefield modelling in strongly scattering media," J. Geophys. Eng. **17**(2), 277–299 (2020).
[11]M. Jakobsen, X. Huang, and R.-S. Wu, "Homotopy analysis of the Lippmann–Schwinger equation for seismic wavefield modelling in strongly scattering media," Geophys. J. Int. **222**(2), 743–753 (2020).
[12]R. K. Saha, S. Karmakar, A. Adhikari, and M. C. Kolios, "Photoacoustic field calculation for nonspherical axisymmetric fluid particles," Biomed. Phys. Eng. Express **3**(1), 015017 (2017).

[13]A. Kaushik, D. Sonker, and R. K. Saha, "Study on angular distribution of differential photoacoustic cross-section and its implication in source size determination," J. Opt. Soc. Am. A **36**(3), 387–396 (2019).
[14]A. Kaushik, A. Paul, and R. K. Saha, "Systematic analysis of frequency dependent differential photoacoustic cross-section data for source size estimation," J. Opt. Soc. Am. A **37**(12), 1895–1904 (2020).
[15]A. Kaushik and R. K. Saha, "Characterization of normal and deformed red blood cells using simulated differential photoacoustic cross-section spectral data," J. Phys. Commun. **5**, 035007 (2021).
[16]P. Mohajerani, S. Kellnberger, and V. Ntziachristos, "Frequency domain optoacoustic tomography using amplitude and phase," Photoacoustics **2**(3), 111–118 (2014).
[17]P. Mohajerani, S. Kellnberger, and V. Ntziachristos, "Fast Fourier back-projection for frequency-domain optoacoustic tomography," Opt. Lett. **39**(18), 5455–5458 (2014).
[18]N. Baddour, "Theory and analysis of frequency-domain photoacoustic tomography," J. Acoust. Soc. Am. **123**(5), 2577–2590 (2008).
[19]N. Baddour and A. Mandelis, "The effect of acoustic impedance on sub-surface absorber geometry reconstruction using 1D frequency-domain photoacoustics," Photoacoustics **3**(4), 132–142 (2015).
[20]B. E. Treeby and B. T. Cox, "k-Wave: Matlab toolbox for the simulation and reconstruction of photoacoustic wave fields," J. Biomed. Opt. **15**(2), 021314 (2010).
[21]D. Chu and Z. Ye, "A phase-compensated distorted wave born approximation representation of the bistatic scattering by weakly scattering objects: Application to zooplankton," J. Acoust. Soc. Am. **106**(4), 1732–1743 (1999).
[22]S. K. Sharma and R. K. Saha, "A new approximate formula for scattering of plane acoustic waves by a spherical obstacle," Acta Acust. Acust. **95**(1), 1–6 (2009).
[23]P. M. Morse and K. U. Ingard, *Theoretical Acoustics* (McGraw-Hill, New York, 1968).
[24]A. Ishimaru, *Wave Propagation and Scattering in Random Media* (Wiley, New York, 2002).
[25]L. I. Schiff, *Quantum Mechanics* (McGraw-Hill Education/Asia, Hong Kong, 1969).
[26]P. M. Morse and H. Feshbach, *Methods of Theoretical Physics* (McGraw-Hill, New York, 1953).
[27]E. M. Strohm, E. S. Berndl, and M. C. Kolios, "Probing red blood cell morphology using high-frequency photoacoustics," Biophys. J. **105**(1), 59–67 (2013).
[28]R. K. Saha, "Photoacoustic-field-calculation," https://github.com/ratank-saha/Photoacoustic-field-calculation (Last viewed December 8, 2020).
[29]R. Prakash, D. Badal, A. Paul, D. Sonker, and R. K. Saha, "Photoacoustic signal simulation using discrete particle approach and its application in tomography," IEEE Trans. Ultrasonics Ferroelectr. Freq. Control **68**, 707–717 (2021).
[30]E. L. Hinrichsen, J. Feder, and T. Jøssang, "Random packing of disks in two dimensions," Phys. Rev. A **41**(8), 4199–4209 (1990).
[31]J. G. Berryman, "Random close packing of hard spheres and disks," Phys. Rev. A **27**(2), 1053–1061 (1983).
[32]N. Metropolis, A. W. Rosenbluth, M. N. Rosenbluth, A. H. Teller, and E. Teller, "Equation of state calculations by fast computing machines," J. Chem. Phys. **21**(6), 1087–1092 (1953).